


RESEARCH

Open Access



Conceptual design of the optical system of the 6.5m wide field multiplexed survey telescope with excellent image quality

Yifan Zhang^{1,2,3*} , Haijiao Jiang^{1,2,4*}, Stephen Shectman⁵, Dehua Yang^{1,2,4}, Zheng Cai^{1,2,4*}, Yong Shi^{6,7}, Song Huang^{1,2,4}, Lu Lu^{1,2,4}, Yamin Zheng^{1,2,3}, Shaonan Kang^{1,2,3}, Shude Mao^{1,2,4} and Lei Huang^{1,2,3*}

*Correspondence:

yifan-zh21@mails.tsinghua.edu.cn;
haijiaojiang@tsinghua.edu.cn;
zcaic@mail.tsinghua.edu.cn;
hl@tsinghua.edu.cn

¹ MUltiplexed Survey Telescope (MUST) Project Collaboration, Tsinghua University, Beijing 100084, China

² Center for Astronomy Technology, Tsinghua University, Beijing 100084, China

³ Department of Precision Instrument, Tsinghua University, Beijing 100084, China

⁴ Department of Astronomy, Tsinghua University, Beijing 100084, China

⁵ Carnegie Institution of Washington, The Carnegie Observatories, Pasadena, CA 91101, USA

⁶ School of Astronomy and Space Science, Nanjing University, Nanjing 210093, China

⁷ Key Laboratory of Modern Astronomy and Astrophysics (Nanjing University), Ministry of Education, Nanjing 210093, China

Abstract

Astrophysics and cosmology in the coming decades urgently need a large field-of-view (FOV), highly multiplexed spectroscopic survey telescope satisfying challenging image quality and stability requirements. The 6.5 m Multiplexed Survey Telescope (MUST) proposed by Tsinghua University will be constructed on the Saishiteng Mountain of Northwest China to improve the spectroscopic survey capability of ground-based optical telescopes. In this paper, we demonstrate the conceptual design of the optical system of MUST. MUST will adopt a 6.5 m primary mirror, a 2.45 m secondary mirror, and a multiple-element widefield corrector (WFC) to ensure excellent image quality with an 80% encircled energy size of image spots less than ~ 0.6 arcsec in diameter for the entire 3° FOV and the whole 50° zenith angle range. Thanks to its compact 6.5 m Ritchey-Chretien system and 20,000 optical fibers on its Cassegrain focus, MUST will carry out state-of-the-art wide-field spectroscopic surveys with efficiency ~ 19 times higher than the Dark Energy Spectroscopic Instrument (DESI) using a measure proposed by Ellis et al. Upon completion around 2029, MUST will be one of the world's most advanced wide-field spectroscopic survey telescopes and a new essential reference for the future development of wide-field survey telescopes. It will enable significant advances in many fields in astrophysics and cosmology.

Keywords: Spectroscopic survey telescope, Ritchey-Chretien system, Cassegrain focus, Field-of-view, Atmospheric dispersion corrector

Introduction

As testified by the multiple Nobel prizes awarded in the last decade, astronomy remains one of the most influential branches of fundamental science and continues to expand the horizon of our understanding of the universe. Ground-based telescopes, including optical and near-infrared ones used for imaging and spectroscopic observations, are still among astronomy's most indispensable observing facilities. To gain a deeper and more detailed view of the universe, the diameter of the primary mirror for ground-based telescopes has dramatically increased to as large as 24.5 m (e.g., Giant Magellan Telescope), 30 m (e.g., Thirty Meter Telescope) and 39 m (e.g., European Extremely Large Telescope)

[1–4] in the last 30 years. At the same time, astronomy now also requires increasingly larger and deeper surveys of the sky, including imaging and spectroscopic ones. Ground- and space-based imaging surveys have provided us with a better view of the universe. For instance, the Cosmological Evolution Survey (COSMOS) [5, 6] using the Hubble Space Telescope (HST) and many ground-based facilities have revolutionized the field of galaxy evolution even though it covers only 2 square degrees of the sky. Meanwhile, spectroscopic survey telescopes with large field-of-view (FOV) and multiplex capability also contribute significantly to the studies of dark energy & dark matter, stellar physics, gravitational wave cosmology, the structure and evolution of our Milky Way, and many other areas.

In the past few decades, various high-quality spectroscopic survey telescopes with large FOV have been designed and built for highly efficient Galactic and extragalactic surveys. For example, the Sloan Digital Sky Survey (SDSS) at the Apache Point Observatory in New Mexico, United States, has released an unprecedented number of new spectra of galaxies, quasars, and stars through its legacy survey and Baryon Oscillation Spectroscopic Survey (BOSS) projects. As a Ritchey-Chretien (R–C) telescope, SDSS uses a primary mirror (2.5 m diameter, conic constant $k = -1.285$), a secondary mirror (1.8 m diameter, conic constant $k = -11.97$), a common corrector, and a pair of interchangeable corrector elements for imaging and spectroscopy respectively near the Cassegrain focus. SDSS can focus 80% encircled energy (EE80) of the image spots within 1.5 arcsec diameter, which offers imaging quality well matched to the 3 arcsec fiber for the entire 3° FOV [7–9]. The Multiple Mirror Telescope (MMT) [10, 11], a joint venture of the Smithsonian Institution and the University of Arizona, represents another meaningful step in multi-object spectroscopy like SDSS. The upgraded MMT is a classical Cassegrain optical system with a 6.5 m diameter primary mirror and a 1.7 m diameter secondary mirror, which provides 1° FOV for spectroscopy and 0.5° FOV for imaging. At the same time, the full-width half maximum (FWHM) of the stellar image is smaller than $0.5''$ under excellent seeing conditions.

Due to the large sample sizes and low systematics needed for understanding the nature of dark energy and dark matter, cosmology surveys have imposed even more demanding requirements on the optical design of spectroscopic survey telescopes. The Dark Energy Spectroscopic Instrument (DESI) is collecting spectra from tens of millions of galaxies and quasars to construct a 3-D map of the universe spanning from our neighborhood galaxies to 11 billion light years away. Taking advantage of the existing primary mirror at the 4-m Mayall telescope, DESI developed a six-lens corrector with diameters ranging from 0.8 m to 1.14 m to replace the previous prime focus corrector and installed 5000 robotic fiber-positioners. DESI has an $F/3.67$ focal ratio and can achieve an EE80 size of image spots less than 0.75 arcsec in diameter for the entire 3.2° FOV when the zenith angle is $< 50^\circ$ [12, 13]. The Subaru telescope, a Japanese 8.2 m R–C telescope operating in Hawaii since 1999 [14–16], has a unique optical design that enables wide-field imaging and spectroscopic capabilities. At Subaru, a novel corrector system compensates the atmospheric dispersion by laterally shifting a pair of lenses off-axis. The Metrology Camera System (MCS) is mounted below the primary mirror at the Cassegrain focus. Exploiting the prime focus capability, the Prime Focus Spectrograph (PFS) is being developed to host 2400 fibers over 1.3° FOV to conduct deep spectroscopic surveys. In

China, the Large Sky Area Multi-Object Fiber Spectroscopic Telescope (LAMOST) has been observing since 2009 at the Xinglong Station of the National Astronomical Observatory of China (NAOC) [17–20]. LAMOST, with an effective aperture of 3.6 m to 4.9 m and a focal length of 20 m at an F/5 focal ratio, uses an active reflecting Schmidt configuration to realize a large FOV of 20 square degrees. Using the parallel controllable fiber positioning technique, about 4000 optical fibers are positioned in a 1.75 m diameter focal plane to carry out the spectroscopic survey. So far it has observed 10 million stars in the Milky Way [21], improving our understanding of the Milky Way.

While the current extragalactic spectroscopic surveys have accumulated more than 20 million spectra of stars and galaxies, future scientific goals require more than 10 billion to fully characterize the cosmology and extragalactic science goals. A significant gap of three orders of magnitudes still exists and demands even more powerful spectroscopic facilities to catch up with the pace of imaging surveys. Tsinghua University has also conceived the 6.5 m MULTiplexed Survey Telescope (MUST, Fig. 1) to survey the northern sky and help achieve this ambitious goal. This telescope is supposed to be located at the Saishiteng Mountain, Qinghai Province of Northwest China (4330 m altitude, 0.6 standard atmospheric pressure, -25°C to 30°C temperature range, 0.75 arcsec median seeing [22]). It will adopt a more compact R–C system with a Cassegrain focus and a multiple-element widefield corrector (WFC) to achieve better dome-seeing and atmospheric dispersion correction. MUST will use high-resolution encoders and DC servo drive motors to control the azimuth and elevation axes and to achieve high-precision positioning and tracking of targets over a 50° zenith angle range. Using a 6.5 m diameter primary mirror and more than 20,000 optical fibers on the focal plane, MUST will carry out state-of-the-art wide-field spectroscopic surveys with efficiency ~ 19 times higher than DESI.

One of the most critical challenges of the MUST is the design and optimization of the R–C system to realize an excellent image quality with an EE80 size of image spots

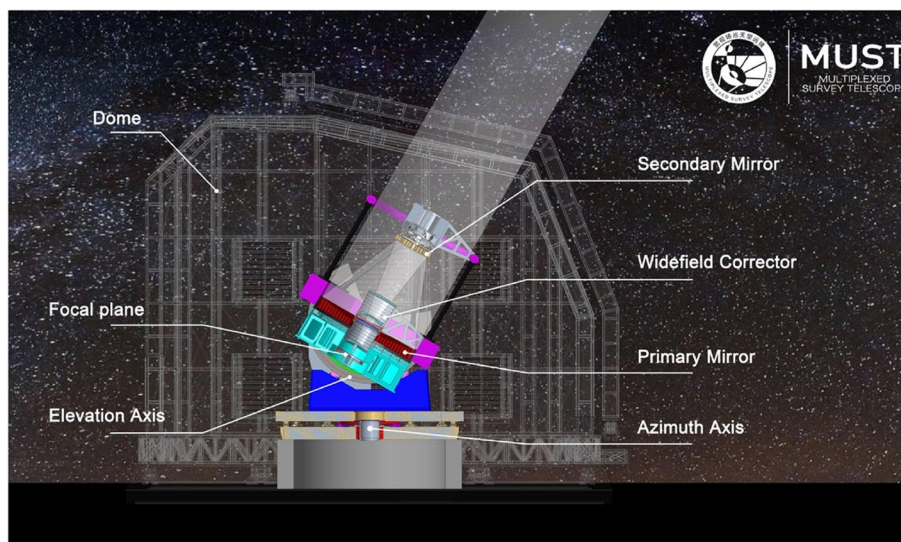


Fig. 1 Schematic of the conceptual design of the 6.5 m MULTiplexed Survey Telescope (MUST)

less than about 0.6 arcsec in diameter for the entire 3° FOV and the whole 50° zenith angle range, with broad wavelength coverage from $0.365\ \mu\text{m}$ to $1.1\ \mu\text{m}$. Meanwhile, the optimization of the mirror materials, the design of the light-weighted mirror and supporting structures, and the development of the control system of the primary & secondary mirrors and the WFC are among the remaining challenges for MUST. Recently, with the rapid development of telescopic optical systems, various important optical designs have been proposed to develop the technologies of the wide-field spectroscopic survey telescopes. Researchers in the University of Arizona have put forward an optical design for a two-mirror 6.5 m telescope with 3° FOV [23]. They designed a refractive corrector with five elements to yield an unvignetted field of 1.284 m diameter at F/3.7 focal ratio. A special designed gull-wing lens corrector with a diameter of 1.56 m is key to controlling the size of the refractor corrector elements to be little more than that of the large image. The images could successfully reach a EE80 diameter of 0.53 arcsec in average over 3° field of view and 40° zenith angle. However, the gull-wing lens is challenging for fabrication and surface measurement due to its strong asphericity and large size. An optical design of the Southern Survey Telescope based on wide-field Cassegrain corrector configuration is proposed by taking the atmospheric dispersion effect of the candidate site and actual science goals into consideration [24]. This design considers the trade-off with respect to the choice of focus type, M2's aperture size, corrector's aperture size, maximum FOV to obtain the optimal configuration of the optical system. By using a couple of rotating zero deviation atmospheric dispersion corrector (ADC) made of LLF1HT and N-BK7 glass material, the atmospheric dispersion effect is well compensated and the superior image quality for a FOV of $2.4^\circ \times 2.4^\circ$ with EE80 diameters less than 0.3 arcsec is successfully achieved. But large size glass made of LLF1HT and N-BK7 and the gluing of lens-prisms bring obstacles to manufacture and cost. In 2021, researchers in Nanjing Institute of Astronomical Optics & Technology have presented four concept optical designs with different correctors for a 6.5 m Cassegrain type multi-objective fiber spectroscopic telescope [25]. By using the corrector composing of 4–5-piece lenses with the maximum diameter of 1.66 m, the four optical systems could reach image quality with the EE80 diameter of less than or equal to 0.60 arcsec. In the proposed system I, the lenses are made of three kinds of materials (i.e., fused silica, Schott BK7HT and LLF1HT). The extra coma introduced by the corrector is small and the secondary mirror is no need to be tilted or decentered during observation. For system II, the material is Schott LLF1HT for ADC and fused silica for other lenses, while the maximum slope of the aspheric lenses is 0.03 and the maximum asphericity of lenses corrector is 2.3 mm. The ADCs in systems I and II are designed to counter-rotate around the optical axis to compensate the atmospheric dispersion, while they laterally shift perpendicular to optical axis in systems III. Different from other three systems, system IV includes four lenses all made of fused silica and one of them serves as ADC to eliminate atmospheric dispersion by lateral shift. These designs are applicable for the telescope to be built at the altitude of 2500 m with the observation wavelength range of $0.365\text{--}0.95\ \mu\text{m}$. However, as the designers point out, the gluing of large size lens is challenging for system I. The processing of large lenses made of LLF1HT and BK7HT poses a challenge to current manufacture technology. In systems II and III, three lenses are designed to be installed behind the primary mirror, which might bring difficulties in spatial layout of the support

system and other following structure. For system IV, the main shortcoming is that secondary mirror and focal surface should be tilted during observation and the tilt angles are not tiny.

In order to achieve the demanding goals of the 6.5 m MUltiplexed Survey Telescope, the optical system is designed to adopt a compact R–C system with a Cassegrain focus and a large WFC to facilitate the required high image quality and survey efficiency, considering material availability, fabrication feasibility, structure reliability and site condition. In this paper, the pivotal breakthrough and innovation in the systematic and comprehensive optical design is presented. A 6.5 m primary mirror, a 2.45 m secondary mirror, and a multiple-element widefield corrector (WFC) is designed to form the optical system. The excellent image quality with an 80% encircled energy size of image spots less than ~ 0.6 arcsec in diameter for the entire 3° FOV and the whole 50° zenith angle range is eventually achieved. The outline of this paper is as follows. In the Method section, we introduce the design and optimization methods, including the model of the optical system and the optimization criteria. Based on these methods, we present the results of the design and optimization of MUST in detail in the Result section. This section includes the design of the optical system, the primary mirror component, the secondary mirror component, and the WFC component. We will also present the image quality and analysis of the thermal effects. In addition, this conceptual design of MUST can serve as an essential reference for future developments of similar projects.

Method

We carry out the conceptual design of the optical system of MUST to achieve its desired scientific goals. We use the Zemax Optic Studio to establish the model of the optical system. The initial setting takes the primary parameters shown in Table 1 as the input. These parameters include the required FOV, wavelength range, as well as environmental temperature and atmospheric pressure of the observation site.

When MUST scans the sky at different zenith angles, it will encounter different atmospheric dispersions. To model this effect, a simplified atmospheric dispersion model is added into the optical system model. This simplified atmospheric dispersion model is a homogeneous vacuum splitter consisting of an air layer and a tilted surface. In this model, the refraction index and Abbe number of the air layer are set 0.99973 and 89.196,

Table 1 Parameters of the optical system model of MUST

Parameter	Requirement
Optical structure	Ritchey-Chretien optics and WFC
Focus type	Cassegrain focus
Wavelength band	0.365 μm to 1.1 μm
Entry aperture	6.5 m
FOV	3° in diameter
Focal ratio	F/3.6
Zenith angle	0° to 50°
EE80 size of image spot	< 0.6 arcsec in diameter
Distortion	$\leq 1\%$
Angle between the incident light and the normal of focal plane	$\leq 1^\circ$

respectively. The air layer is defined extending from infinity to the tilted surface and the inclination angle of the tilted surface is set varying with the zenith angle. Thus, the properties of the light passing through the atmosphere at different zenith angles before entering the optical system can be accurately simulated. The R–C system cooperating with the WFC is selected as the main optical structure instead of a Prime focus system. Light rays are converged at the Cassegrain focus after passing through the R–C system which is more stable under gravity when heavy optical equipment such as a spectrometer or corrector are required in the subsequent light path. Since the length of the telescope barrel of the R–C system is only about 2/3 of that for a Prime focus system, it allows a more compact structure that requires a smaller dome. Furthermore, in order to effectively depress the spherical aberration and coma, hyperboloid primary and secondary mirrors are adopted in the R–C system [26].

As a wide-field, fiber-fed massive spectroscopic survey telescope, MUST is expected to revolutionize our ability to map the universe. Robots (fiber positioners) and a spectrograph have been designed for this telescope to simultaneously capture light from a large number of galaxies. The light will be focused into multi-mode optical fibers held by the robots and guided into the spectrograph. The coupling efficiency and focal ratio degradation (FRD) of optical fibers affect the overall efficiency of the telescope and in turn affect the survey depth and spectral accuracy. Both parameters are related to the focal ratio of the telescope, which is the basis of the overall design of the entire telescope and determines the initial structure and overall layout of the telescope. A proper focal ratio should be achieved at the beginning of the optical system design. Different from the ideal state of optical fibers, where the incident angle is the same as the exit angle, FRD indicates that the focal ratio of the light will become faster after passing through optical fibers, which could be caused by factors including surface irregularities in the inner wall of optical fibers, diffraction, the stress in fibers, and polishing errors on the end surface [27]. Under the effect of FRD, focal ratio will be reduced after passing through optical fibers. In order to match this new focal ratio, focal ratio of spectrograph collimator should be adjusted to get the same spectral resolution and the fiber number. Related to the focal ratio and fiber types, previous works have demonstrated that the FRD is at its lowest when the focal ratio is between F/3 and F/4 [28, 29]. While a slower focal ratio can help improve imaging performance, a faster focal ratio helps limit the physical size of the corrector elements and the focal plane assembly. Based on these considerations, the focal ratio of the MUST is set between F/3.5 and F/3.7 after balancing the performance and the cost.

Based on the above reasoning, we choose to use an R–C structure telescope with an F/3.6 Cassegrain focus as the baseline design for the optical system model. We calculate the initial parameters for this design and apply them in the lens data editor before optimization. The focal length (f_1) of the primary mirror and the magnification of the secondary mirror (β) can be obtained from the known focal ratio and diameter of the primary mirror. Considering that the primary mirror support, thermal control systems, and the corrector assembly occupy a certain amount of space, the position of focal plane needs to be set far enough behind the primary mirror. As the geometric relationship shown in Fig. 2, the distance (d) between the primary mirror and the secondary mirror can be written as Eq. (1), and the radius of the secondary mirror can be expressed as

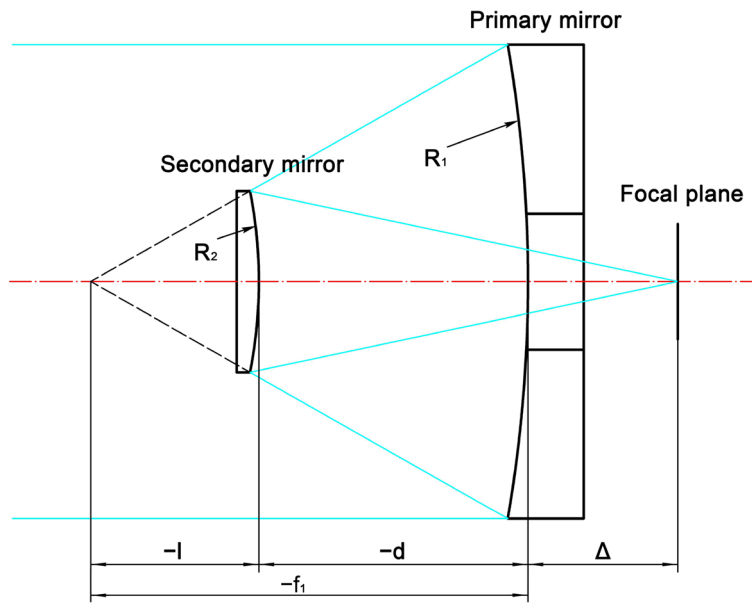


Fig. 2 Initial parameters of the R-C optical system with the Cassegrain focus

Eq. (2). The conic constants of the primary and secondary mirrors (k_1 and k_2) are set to eliminate the spherical aberration and coma, which are expressed as Eq. (3) [30, 31].

$$d = f_1 - l = f_1 - \frac{f_1 + \Delta}{\beta - 1} \tag{1}$$

$$R_2 = \frac{\alpha\beta}{\beta + 1} R_1, \alpha = \frac{l}{f_1} \tag{2}$$

$$k_1 = -1 - \frac{2\alpha}{(1 - \alpha)\beta^2}, k_2 = \frac{\frac{2\beta}{1 - \alpha} + (1 + \beta)(1 - \beta)^2}{(1 + \beta)^3} \tag{3}$$

In Fig. 2 and Eqs. (1)-(3), d is the distance between the primary mirror and secondary mirror, f_1 is the focal length of primary mirror, l is the distance between the focal point of the primary mirror and the secondary mirror, Δ is the distance between the primary mirror and focal plane; β is the magnification of the secondary mirror, R_1 is the radius of curvature of primary mirror, R_2 is the radius of curvature of secondary mirror, k_1 is the conic constants of primary mirror, and k_2 is the conic constants of secondary mirror. After setting the initial parameters, we adopt the Hammer Optimizer method and Damped Least Squares (DLS) algorithm to optimize the optical system. Equation (4) below shows the merit function for the optimization iteration. This merit function uses the spot radius to evaluate the image quality.

$$MF(x_1, x_2, \dots, x_N)^2 = \frac{\sum W_i [V_i(x_1, x_2, \dots, x_N) - T_i]^2}{\sum W_i} \tag{4}$$

where x_1, x_2, \dots, x_N represent different variables of the optical system, V_i represents the current value calculated by Zemax Optic Studio, W_i represents the absolute value of the weight of these operands, and T_i represents the target value. At the same time, the center thickness, edge thickness, and asphericity of the aspheric surface are restricted within a preset range during the iteration. In addition, as an array of optical fibers with a diameter of $150 \mu\text{m}$ is placed on the focal plane to transmit the light to the spectrographs, the optimized image quality should match the size of the optical fiber, while the EE80 size of the image spot and the image distortion are limited not to exceed 0.6 arcsec and 1% respectively to avoid the crosstalk between adjacent spectrums on the focal plane of the spectrographs. To reduce the loss of light when entering the optical fiber, the angle between the incident light and the normal of the focal plane is constrained to be smaller than 1° . Optimizing the optical system starts from the initial input values and then we iterate based on Eq. (4) until the final results are reached. We should note that to ensure the validity of the iteration, it is possible to keep adjusting both variables and operands while repeatedly checking output values of the RMS radius, distortion, EE80 size, and other indicators of the light spots.

Results

Optical system overview of the MUST

Based on the above optical system model and iteration criteria, the conceptual design and optimization of the optical system of MUST are obtained as shown in Fig. 3, Tables 2 and 3. The results include the design of a compact R-C system with Cassegrain focus along with all of its mirror components (i.e., the primary mirror, the secondary mirror, and the WFC). As shown in Fig. 3a, a concave hyperboloid primary mirror (6.5 m diameter, M1) with a central hole (1.8 m diameter) and a convex

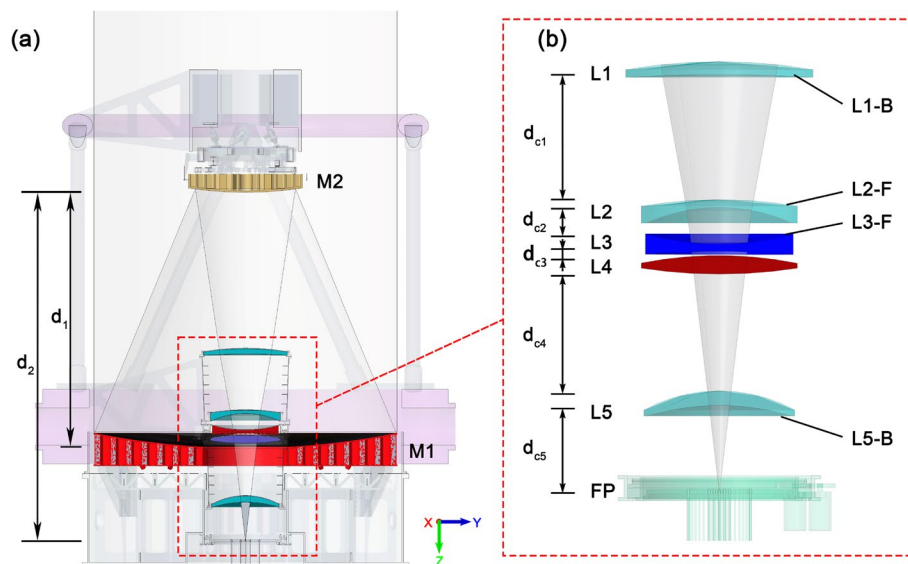


Fig. 3 **a** Schematic of the designed optical system of MUST. M1 is the primary mirror, and M2 is the secondary mirror. **b** The WFC consists of lenses L1 ~ L5. The back surface of L1 (L1-B), the front surface of L2 (L2-F), the front surface of L3 (L3-F), and the back surface of L5 (L5-B) are aspheric. d_1 is the distance between primary mirror and secondary mirror, d_2 is the distance between secondary mirror and focal plane. d_{c1} , d_{c2} , d_{c3} , d_{c4} , d_{c5} are the distance between L1, L2, L3, L4, L5 and focal plane respectively

Table 2 Optical parameters of the primary mirror, secondary mirror, WFC, and focal plane

Surface	Radius (mm)	Thickness (mm)	Material	Mech Semi-Dia (mm)	Conic
M1	-16,256.000	-5500	MIRROR (Ohara E6 Borosilicate)	3251.2	-1.219518
M2	-8302.487	3350	MIRROR (Zerodur glass)	1225.0	-7.585198
L1-F	5224.476	125	SILICA	900.0	-
L1-B	15,259.604	1200		900.0	-
L2-F	4332.628	80	SILICA	750.0	-
L2-B	1748.227	350		750.0	-
L3-F	-2535.230	70	SILICA	745.0	-
L3-B	8465.709	40		745.0	-
L4-F	3860.132	180	SILICA	750.0	-
L4-B	-4903.155	1120		750.0	-
L5-F	1510.265	140	SILICA	725.0	-
L5-B	2514.536	700		725.0	-
FP	-9216.780	-	IMAGE	615.3	-

Table 3 Aspheric surfaces of the WFC and focal plane

Surface	4 th	6 th	8 th	10 th	Maximum depth to remove (mm)
L1-B	3.400E-12	-2.230E-18	5.985E-25	-4.647E-32	0.21
L2-F	-1.058E-13	-9.539E-18	-3.779E-24	1.916E-29	0.30
L3-F	7.675E-2	3.148E-18	-2.215E-24	-2.337E-29	0.40
L5-B	1.388E-11	-1.409E-17	-1.576E-23	-1.450E-30	0.51
FP	-1.254E-11	6.264E-17	-1.899E-22	1.801E-28	-

hyperboloid secondary mirror (2.45 m diameter, M2) with 5500 mm apart (d_1) form the basic R-C optical system with a focal ratio of F/3.6 and a total focal length of 23323 mm. Considering the material availability and fabrication feasibility, the WFC (i.e., L1-L5) will be manufactured entirely using fused silica. Only four surfaces of the WFC are designed as aspheric surfaces with relatively low asphericity (see Fig. 3b and Table 3). A counter-rotating type ADC consisting of lenses L3 and L4 is used to compensate for the atmospheric dispersion when the telescope scans the sky at different zenith angles. The mechanical diameters of each lens of the WFC are set as 1.8 m, 1.5 m, 1.49 m, 1.5 m, and 1.45 m. And the intervals between two adjacent lenses (i.e., d_{c1} - d_{c4}) are 1200 mm, 350 mm, 40 mm, and 1120 mm, respectively. In practice, as the diameter of lens L1 is almost the same as that of the central hole of the primary mirror, lens L2-L5 will be assembled into a single structure and installed in the mirror cell (Fig. 3a) as the first step. Lens L1 will then be subsequently installed from above. Using the designed optical system, MUST will achieve an excellent image quality with an EE80 size of image spots less than 0.6 arcsec in diameter for the entire 3° FOV and over a 50° zenith angle range. Figure 3 illustrates where the image spots will enter the optical fibers positioned at the focal plane [700 mm (i.e., d_{c5}) away from lens L5]. The fibers will be connected to multi-object spectrographs that will collect spectra ranging from 0.365 μm to 1.1 μm .

By utilizing the compact R–C configuration, the full height of the telescope could be limited to <7230 mm to achieve better dome seeing. During operation, the wavefront aberration caused by mirror gravity, mirror displacement and tilt, structural stress, and temperature difference will be compensated by the primary mirror's deformed surface shape and the secondary mirror's adjustment. MUST can focus the high-quality spots into the densely packed 20,000 optical fibers on the focal plane.

Primary mirror

In the optical system of MUST, the primary mirror is designed as a honeycomb-shaped lightweight single mirror instead of a segmented mirror to improve image quality and reduce control complexity. As shown in Table 2 and Fig. 4, the 6.5 m primary mirror with a circular hole in the center is a hyperbolic concave-flat mirror with a curvature radius of -16256 mm, the conic constant of -1.22 and it weights 8 tons. The material of primary mirror is Ohara E6 borosilicate with a linear expansion coefficient of $2.8 \times 10^{-6} \text{ K}^{-1}$. Figure 4a is the machining drawing of the primary mirror, which presents the detailed geometric dimensions of the diameters of the front and back surface (6512.6 mm and 6471.9 mm), the front and back diameters of the central hole (1800 mm and 1815.2 mm) and the thicknesses of the edge and the central hole (711.2 mm and 385.1 mm), respectively. During operation, various factors (e.g., gravity, temperature variation, and wind) will introduce deformations to the surface shape of the primary mirror and thereby affect the image quality. To compensate for the aberration and maintain the surface quality, the primary mirror will be installed in the cell (Fig. 4b), an active support system is equipped to adjust the surface shape at each zenith angle dynamically. Figure 4c shows the 100 load spreaders arranged at the back of the primary mirror, which are connected to the active support in the mirror cell. Considering the operation temperature at the Saishiteng Mountain (varying from -25°C to 30°C), a thermal control system installed inside the mirror cell will adjust and maintain the temperature of the primary mirror consistent with the ambient temperature. Moreover, the primary mirror is supported by a hexapod that connects the hard points on the primary mirror to the telescope cell. This forms a positional hexapod that is stiff but supports very small forces. The 100 actuators connecting with the load spreaders are used to support and position the primary mirror. The hexapod easily can take large temperature changes. The actuators have a travel budget (laterally 10 mm & axially 8.8 mm) that allows for the motion of the primary mirror that also accommodates temperature changes, mirror position and seismic events.

As shown in Fig. 4d, a finite element analysis model is built to simulate this large-scale primary mirror's surface shape and correction ability. The mirror will be polished and tested on the same pattern of load spreaders as in the telescope, the astigmatism in

(See figure on next page.)

Fig. 4 **a** Sectional machining drawing of the primary mirror with the honeycomb-shaped light-weighted structure. The marked dimensions are the geometric dimensions in actual production. **b** Schematic diagram of the primary mirror and the mirror cell. **c** 100 load spreaders are arranged at the back of the primary mirror. **d** Finite element analysis model of the primary mirror. **e** and **f** Gravity-induced surface deformation at the zenith and horizontal directions. **g** and **h** Surface residuals after being compensated in the zenith and horizontal directions. **i** The latest update on the manufacturing progress of the primary mirror at the Mirror Lab of the Steward Observatory, University of Arizona: the recently cast 6.5 m blank out of the furnace and in good condition

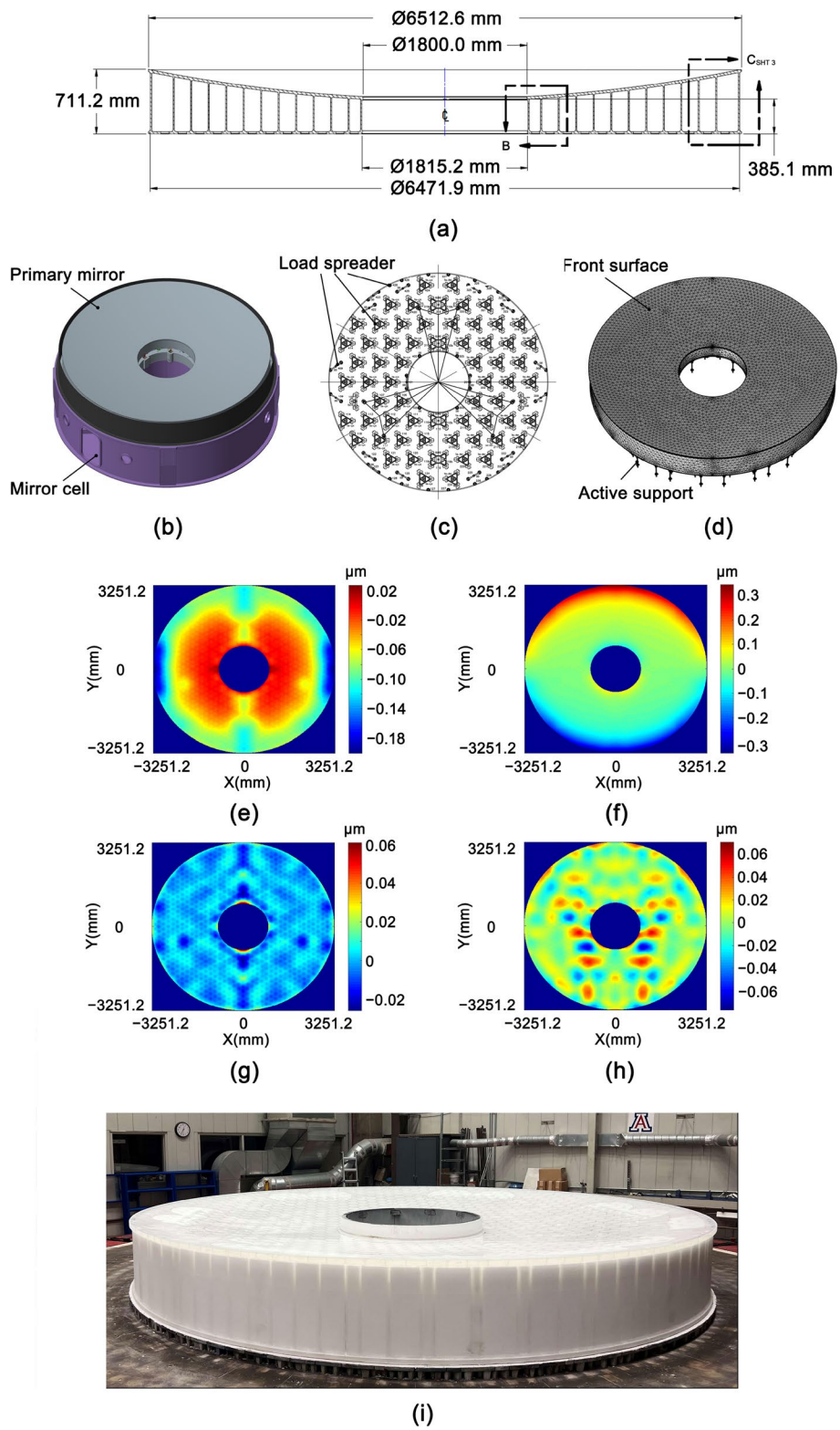


Fig. 4 (See legend on previous page.)

zenith-pointing support is subtracted off zenith-pointing support in the actual processing. What is analyzed here is the situation under the ideal mirror support without considering the actual polishing. Figures 4e and f show the surface deformations caused by the gravity in the zenithal and horizontal pointing, respectively. In the zenith direction, the surface shape is mainly characterized as astigmatism and defocus with the peak-to-valley (PV) value of $0.2268\ \mu\text{m}$ and root-mean-square (RMS) value of $0.041\ \mu\text{m}$, while the surface shape at the horizontal direction is mainly coma aberration with a PV value of $0.6865\ \mu\text{m}$ and an RMS value of $0.096\ \mu\text{m}$. These gravity-induced aberrations could be well compensated by controlling the surface shape through the active support system. As shown in Fig. 4g and 5h, 85.8% of the distortion in the zenith direction is depressed, and the PV and RMS values of the correction residual are $0.086\ \mu\text{m}$ and $0.0058\ \mu\text{m}$. At the same time, 84.4% of the distortion in the horizontal direction is decreased, and the PV and RMS values of the residual are $0.1476\ \mu\text{m}$ and $0.015\ \mu\text{m}$.

According to the detailed design, the primary mirror and the mirror cell are manufactured at the Mirror Lab of the Steward Observatory, University of Arizona. The primary mirror and cell integration will be precisely adjusted when manufactured and assembled to ensure excellent performance under different zenith angles and working temperatures. It is worth noting that, in the optical system of MUST, the primary mirror will be the reference to the assembly of the secondary mirror and the WFC.

Secondary mirror

The secondary mirror is combined with the primary mirror to form the R–C telescope with Cassegrain focus to achieve high image quality in a compact structure. As shown in Fig. 5a, the secondary mirror is designed as a hyperbolic flat-convex mirror (2.45 m diameter, 300 mm thickness at the edge) with a curvature radius of $-8302.487\ \text{mm}$ and a conic constant of -7.585 . To decrease the thermal effect under a wide range of

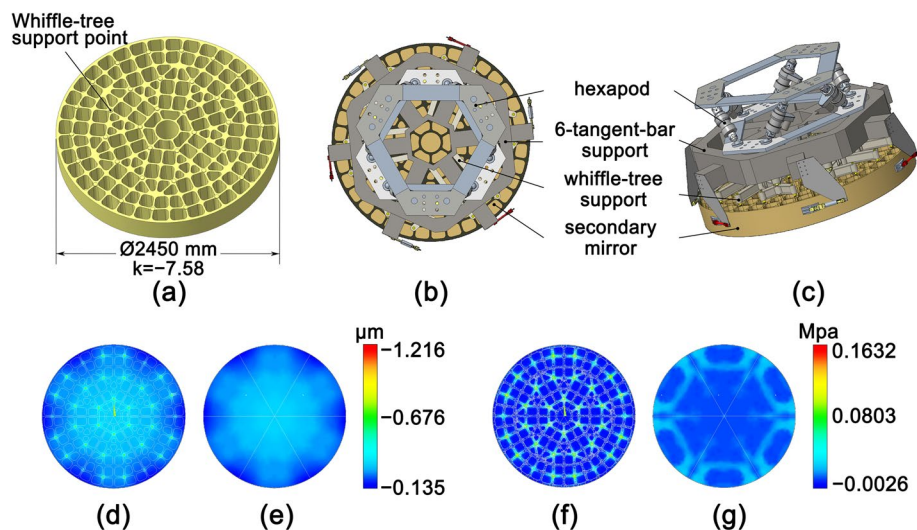


Fig. 5 **a** Schematic of the 2.45 m lightweight secondary mirror with 36 whiffle-tree passive support points at the back, which is designed together with Schott. **b** and **c** Schematic of the conceptual design of the passive support and hexapod of the secondary mirror. **d** and **e** Surface deformation of the front and back surfaces of the secondary mirror under the gravity effect at the zenith direction. **f** and **g** Force distribution of the front and back surfaces of the secondary mirror under the gravity effect at the zenith direction

environmental temperatures, the Zerodur with zero thermal expansion coefficient is chosen as the material of the secondary mirror. To effectively reduce the total weight to under 1 ton, the secondary mirror adopts a light-weighted structure with a ~75% light-weighting ratio (Fig. 5a). Like the primary mirror, the secondary mirror is coated with the aluminum film with a reflectivity of >90% from 0.365 μm to 1.1 μm to improve the optical efficiency.

As shown in Figs. 5b and c, there is a 36-point whiffle-tree for axial support and a 6-tangent-bar for lateral support designed and mounted on a hexapod along with the secondary mirror in current preliminary scheme. This design will reduce the component's overall complexity and ensure the functions for rigid motion adjustment in five dimensions (i.e., piston or focus, tip/tilt, and decenter). Besides the hexapod, there are other ways to achieve high-precision adjustment by deploying 5 actuators to constrain 5 degrees of freedom. Figures 5d-g present the preliminary finite element analysis results of the secondary mirror on the 36-point passive support under the gravity effect in the zenith direction. The surface deformations of the secondary mirror affected by the passive support are as small as 46 nm RMS, and the maximum support force in the mirror is only 0.16 MPa. We should point out that, in the optical system of MUST, when the ADC rotates to eliminate the atmospheric dispersion, the secondary mirror will simultaneously shift along and deflect around the axis to compensate for the aberration caused by the rotation of the ADC and the deviation of the WFC.

Multiple-element widefield corrector

Based on the R-C configuration consisting of a 6.5 m primary mirror and a 2.45 m secondary mirror, the WFC is designed to achieve excellent imaging quality within the entire 3° FOV covering a 50° zenith angle range by compensating the atmospheric dispersion and wavefront aberration. As shown in Fig. 6a, five pieces of lenses (L1 ~ L5) in total make use of the WFC. All the lenses in the WFC will use the same material (i.e., fused silica) to improve the image quality and match the manufacturing feasibility of the lens blanks. Table 3 shows the detailed aspheric coefficients of the four aspheric surfaces, including the back surface of lens L1 (L1-B), the front surface of lens L2 (L2-F), the front surface of lens L3 (L3-F), and the back surface of lens L5 (L5-B). We need to emphasize that lens L1, with a diameter of 1.8 m (the largest lens in the WFC), is currently the largest transmissive corrector element in the world. To improve the optical efficiency and suppress the ghost images, all the corrector elements are coated with the single-layer magnesium fluoride film in high transmissivity (>97% @ 0.365 μm -1.1 μm).

In the WFC, lenses L3 and L4 form the ADC system to correct the radial chromatic aberration caused by the atmospheric dispersion for high image quality. As shown in Fig. 6b, the back surface of lens L3 and front surface of lens L4 are tilted by 0.1148° and 0.1178° , respectively, and thus L3 and L4 form a pair of wedge lenses, which act as the prism that disperses the input light by wavelength. Drive motors control the rotation of lenses L3 and L4 in the opposite directions to generate the dispersion required to correct the atmospheric dispersion during survey observation, as shown in Fig. 6c. As the atmospheric dispersion varies across the sky, the rotating angle of the ADC will also change according to the zenith angle of the telescope. In practice, the driving motors of the ADC and the secondary mirror are jointly operated by the telescope control system

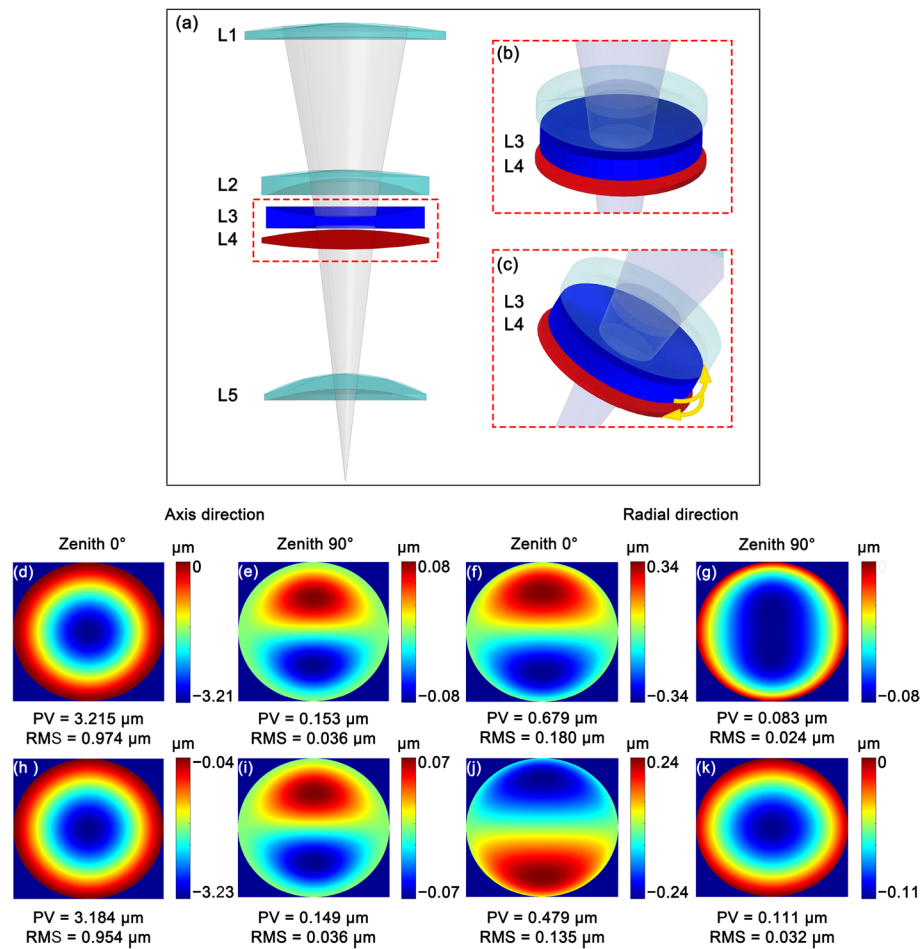


Fig. 6 **a** Schematic of the designed WFC of MUST. **b** The ADC consists of two wedged lenses, L3 and L4. **c** L3 and L4 will rotate in opposite directions to compensate for the atmospheric dispersion. **d**~**g** Deformations of the front surface of lens L1 caused by the gravity in the axial and radial directions at the 0° and 90° zenith angles. **h**~**k** Deformations of the back surface of lens L1 caused by the gravity in the axial and radial directions at the 0° and 90° zenith angles

to maintain image quality and stability. The axial chromatic aberration is compensated by positive and negative lenses in the multiple-element widefield corrector. Lenses L1 and L5 of the WFC are set positive meniscus lenses, while L4 is set a positive biconvex lens. These three lenses will introduce negative axial chromatic aberration. Lenses L2 and L3 are set negative meniscus lenses and will introduce positive axial chromatic aberration. The positive and negative chromatic aberrations are designed to offset each other and the axial chromatic aberration is well compensated.

In the WFC, a flexible circumferential structure supports these 5 pieces of lenses to decrease the mirror deformations and maintain the surface shapes. As an example, Figs. 6d-k show the surface deformations of lens L1 in the axial and radial directions, which are introduced by gravity at the 0° and 90° zenith angles. When the telescope points at the zenith, the aberration caused by the surface deformation mainly defocuses in the axial direction and coma in the radial direction. Meanwhile, when pointed horizontally, the aberration is mainly coma in the axial direction and defocusing in the radial

direction. It should be noted that the influence of surface deformation on the image quality will be further analyzed in Zemax Optic Studio. If necessary, the secondary mirror will shift along and deflect around the axis to compensate for the aberration. During the construction of MUST, the WFC will first be assembled off-site and then installed through the central hole of the primary mirror.

Along with the primary and secondary mirrors, the WFC will improve the image quality of MUST by suppressing atmospheric dispersion and wavefront aberration. However, as the largest corrector element in the world, the lens L1 with a 1.8 m diameter still faces enormous challenges in both material availability and fabrication. The uniformity and homogeneity of the large mirror blank are challenging issues. Currently, the MUST team is discussing with Corning to identify a feasible technical solution that suits the manufacturing progress of the WFC.

Focal plane

After passing through the compact R-C optical system, the target light beams are focused into high-quality image spots with an EE80 diameter smaller than ~0.6 arcsec. They will then enter the 20,000 fibers positioned on the focal plane. The focal plane is connected to multi-object spectrographs to collect the spectra. As shown in Figs. 7a and

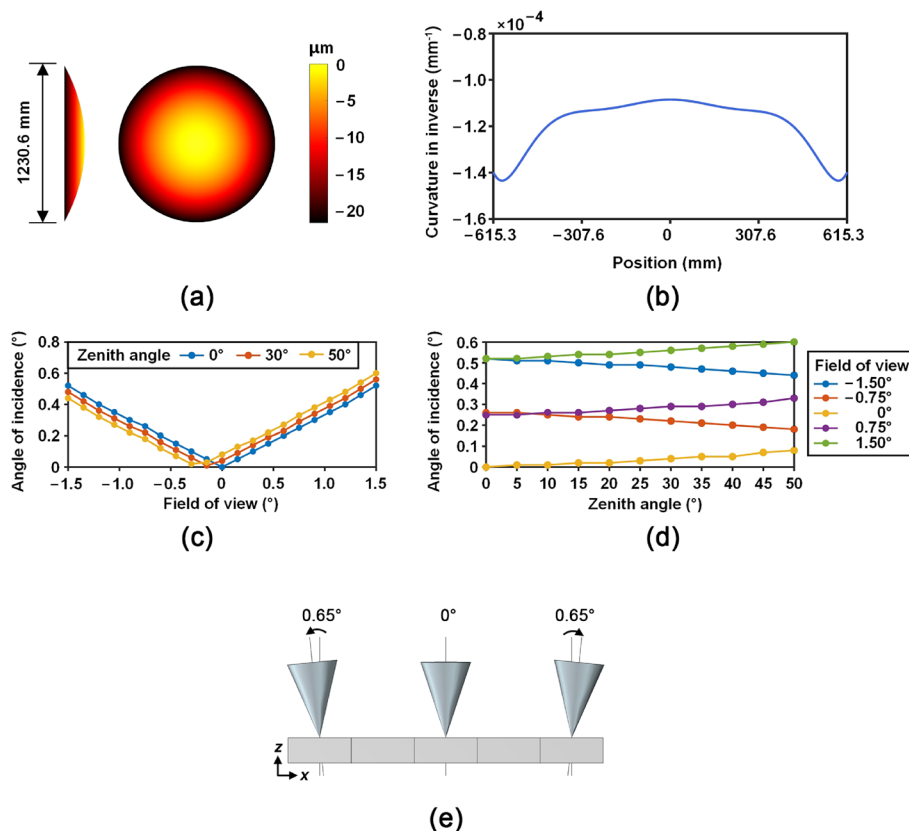


Fig. 7 **a** Vertical view of the surface shape of the focal plane. **b** Sectional drawing of the aspheric surface of the focal plane. **c** Variation of the angle of incidence with the FOV. **d** Variation of the angle of incidence with the zenith angle. **e** Schematic diagram of the angle of incidence between the fiber normal and the incident light in the focal plane, and 0.65° angle of incidence at 50° zenith angle

b, the focal plane is designed as a high-order aspheric surface (the aspheric coefficients are listed in Table 3) with the curvature of -9216.8 mm and the diameter of 1230.6 mm to reduce the FRD over the 3° FOV and 50° zenith angle range. Figures 7c and d show the variation of the incidence angles across the FOV and with the zenith angle. We optimize these angles in the model to ensure the quality of the spectra. As the zenith angle varies, the angle of the incident light also varies within a less than $\pm 0.1^\circ$ range over the entire FOV. When the zenith angle is 50° , the light beam at the edge of the FOV reaches the maximum angle of incidence value at 0.65° (Fig. 7e). Even under this worst case, it has a negligible impact on the vertical incidence for the optical fiber (0.1% deterioration on the EE80 diameter).

Considering the $F/3.6$ focal ratio of the R–C system and the angle of incidence, the core diameter and numerical aperture of each fiber are designed to be 1.3 arcsec (i.e., a 150 μm diameter) and 0.22 (i.e., 25.4° aperture angle) to ensure high coupling efficiency and spectral resolution of 5000 . The $20,000$ optical fibers will be installed onto a high-density fiber positioning device in the focal plane. Each fiber could target any location within the patrol radius of its positioner. Additionally, the focal plane is mounted on a de-rotation platform. The platform will control the focal plane to rotate in the opposite direction to eliminate the image shift caused by the Earth's rotation during exposure.

Image quality

As mentioned earlier, the light from the target is focused by the 6.5 m primary mirror and the 2.45 m secondary mirror, then corrected by the WFC to form a high-quality image spot on the focal plane. Figure 8 shows the performance of the focused image spot for the whole optical system. This includes the spot patterns, the variation curve of the RMS spot radius, the distribution of the RMS spot radius across the entire FOV, and the enclosed energy across the FOV and at different zenith angles. It is worth mentioning that, considering the image quality at the edge of FOV and the size of the lens blanks, the FOV within $\pm 1.275^\circ$ has a central obscuration of 16.12% (Fig. 8q), and we artificially introduced an additional 1.5% vignetting at the edge when modeling the optical system to improve the fidelity of the simulation.

For the 0° zenith angle (Fig. 8a), as shown in Figs. 8d and g, the maximum RMS radius of the image spot within the wavelength range between 0.365 μm and 1.1 μm could be as small as 21.1 μm . This indicates that the atmospheric dispersion and wavefront aberration are effectively controlled. In particular, the RMS radii of all the polychromatic spots are smaller than 19 μm within the central 1.8° (i.e., $\pm 0.9^\circ$) of the FOV. The minimum RMS value can be restricted to as small as 16.4 μm . When the zenith angles are 30° (Fig. 8b) and 50° (Fig. 8c), the atmospheric dispersion and wavefront aberration are also well compensated and corrected by the counter-rotation of the ADC and the WFC. According to the spot diagrams for the 30° zenith angle illustrated in Fig. 8e and h, the RMS radii of all the polychromatic spots are smaller than 25 μm , although it increases quickly toward the edge of the FOV. The RMS radii are still smaller than 20 μm within the central 1.2° (i.e., $\pm 0.6^\circ$) of the FOV. At the maximum zenith angle of 50° for MUST, the RMS radii of the polychromatic spots can also be well controlled within 22.3 μm with a minimum size of 16.6 μm at the center of the FOV (Fig. 8f and i). The distributions of the RMS spot radius for the three zenith angles are shown in Fig. 8j, k, and l.

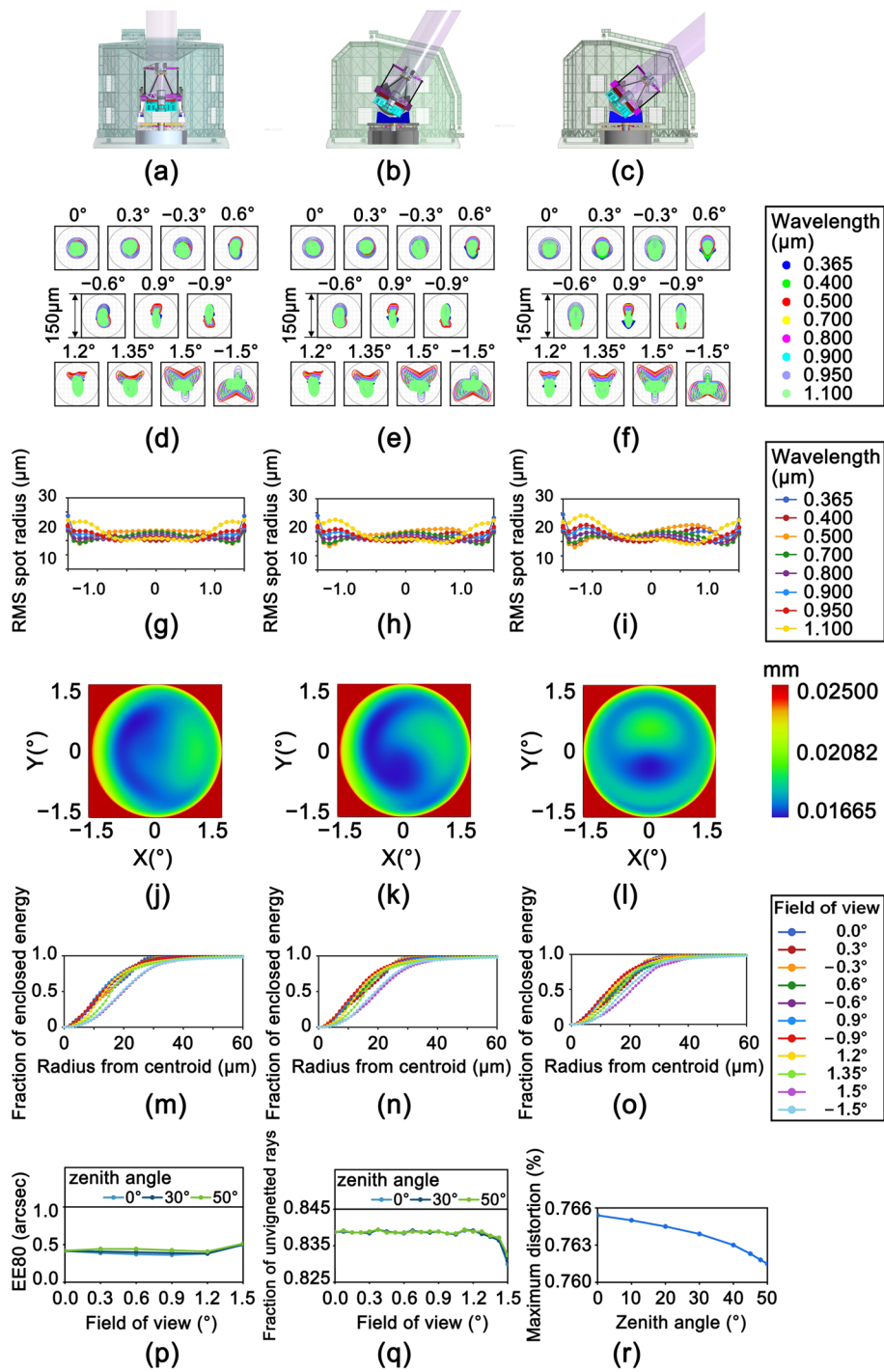


Fig. 8 **a-c** MUST at 0°, 30°, and 50° zenith. **d-f** Spot patterns in the 3° FOV at the three zenith angles. The reference circle is in the dimension of 150 μm (or 1.3"). **g-i** RMS radius of the image spot in the entire 3° FOV at the three zenith angles. **j-l** Distribution of RMS spot radius in the entire 3° FOV at the three zenith angles. **m-o** Fraction of the enclosed energy ranging with the spot radius at the three zenith angles. **p** EE80 diameter ranging with the FOV at different zenith angles. **q** Fraction of unvignetted rays. **r** Maximum distortion at different zenith angle

These figures suggest that the image spots are reasonably uniform across the 3° FOV and within the allowed zenith angle range. Furthermore, we calculated the characteristics of the EE80 of the focused image spot, which is an important indicator in evaluating the concentration of the image. Figure 8m - o show the variations of enclosed energy across the FOV when the zenith angle is 0° , 30° , and 50° . Figure 8p shows the variation of the EE80 diameter versus the position of the FOV. Over the entire FOV and the 50° zenith angle range, the EE80 diameters are smaller than 0.512 arcsec, and the minimum value can reach as low as 0.362 arcsec. The image spot perfectly matches the fiber with a $150\ \mu\text{m}$ core diameter (equal to 1.3 arcsec @ $0.0088\ \text{arcsec}/\mu\text{m}$) and ensures the spectra from adjacent fibers will not interfere with each other. As shown in Fig. 8r, the maximum distortion ranging is below 0.77% with the zenith angle varying from 0° to 50° , which meets the distortion requirement of less than 1% (see Table 1) and could ensure the image quality at the edge of the FOV. Additionally, as the WFC is composed of five large size fused silica lenses, it is possible that the stray lights brought by residual reflections between lens surfaces would form ghost images near or on the focal plane. For this consideration, we have conducted sequential analysis of the optical system by using the Zemax Optic Studio. According to the simulation results, the nearest ghost image, at the position of 28.76 mm away from the focal plane, is formed by the reflection between the back surface of lens L3 and the front surface of lens L1. The total image intensity of the ghost image is as weak as 0.041% of the target signal.

These results confirm that the WFC with an ADC can compensate for the atmospheric dispersion and image aberration. While the primary mirror of MUST is 1.5 times larger than DESI, it can still collect data with an even better image uniformity over the entire FOV. The excellent optical performance allows MUST to survey the entire northern sky with uniform spectral quality efficiently. This reference design can enable exciting science and guide the future development of spectroscopic survey telescopes.

Thermal effect

As mentioned above, MUST will be sited on the Saishiteng Mountain in Northwest China, where the temperature range is as wide as 55°C ranging from -30°C to 25°C . A thermal effect analysis covering such a wide range of temperatures is critical. It can help us assess the stability of image quality and guide the subsequent improvement of the telescope. In the thermal model of the optical system, the variation of the environmental temperature is considered after ignoring its inhomogeneous spatial distribution. The changes in the shape of optical elements and the intervals of optical elements caused by the thermal expansions of the optical materials are the major issues that can degrade the image quality.

To ensure the thermal stability of the image quality of the optical system, all the WFC lenses will be made of fused silica with the desirable uniformity. According to the spot diagrams demonstrated in Fig. 9, the minimum RMS radius of the polychromatic spot for the 0° zenith angle is $16.0\ \mu\text{m}$ ($16.2\ \mu\text{m}$), and the maximum value is $21.4\ \mu\text{m}$ ($21.5\ \mu\text{m}$) at -30°C (25°C). The RMS spot radii are slightly worse and both smaller than $25\ \mu\text{m}$ for the 30° and 50° zenith angles, which indicates that stable image quality could be guaranteed at different zenith angle and different ambient temperature. The image quality analysis in the previous section is based on the optical system model at 2°C , which is the

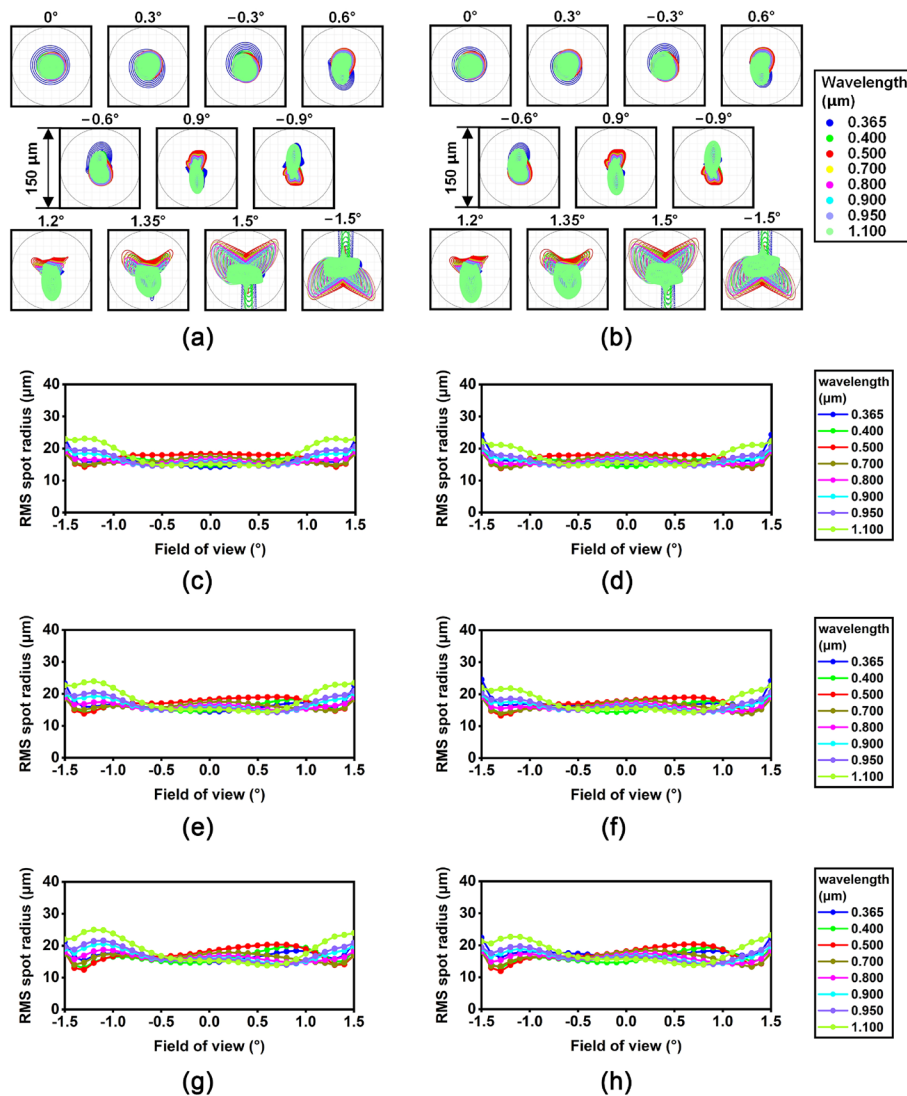


Fig. 9 Spot diagrams for the 0° zenith angle in -30°C (a) and 25°C (b). RMS radius ranging with the FOV for the 0° zenith angle in -30°C (c) and 25°C (d). RMS radius ranging with the FOV for the 30° zenith angle in -30°C (e) and 25°C (f). RMS radius ranging with the FOV for the 50° zenith angle in -30°C (g) and 25°C (h)

average temperature of the observing site. The spot radius and shape at -30 °C and 25 °C are similar to those at the average temperature of 2 °C. And under these extreme temperatures, the behaviors of the image spots are also as expected: the spots close to the center of the FOV are smaller, and those close to the edge of the FOV become slightly larger. Therefore, the environmental temperature variation has little effect on the image quality. Under the allowed temperature range, MUST will have consistently high image quality. It is also worth mentioning that the small thermal impact on the shape and relative positions of the lenses can be further compensated by shifting and deflecting the secondary mirror to achieve even better image quality.

Table 4 Assembly tolerance of the optical system

Element	DX/DY (mm)	DZ (mm)	TX/TY (arcmin)
M2	± 0.020	± 0.05	± 0.10
L1	± 0.200	± 0.50	± 1.00
L2	± 0.100	± 0.40	± 1.20
L3	± 0.125	± 0.48	± 0.90
L4	± 0.100	± 0.30	± 0.90
L5	± 0.200	± 0.45	± 0.90

Table 5 Fabrication tolerance of the optical element

Surface	Curvature radius of the front surface (mm)	Curvature radius of the back surface (mm)	Thickness (mm)	DX/DY (mm)	TX/TY (arcsec)	Surface accuracy	Refraction index	Abbe number	Conic constant
M1	± 3.00	-	-	-	-	$1/20\lambda$	-	-	± 0.0002
M2	± 1.10	-	-	-	-	$1/20\lambda$	-	-	± 0.0005
L1	± 0.75	± 2.00	± 0.45	± 0.10	± 15	$1/10\lambda$	± 0.0005	± 0.10	-
L2	± 1.00	± 1.00	± 0.50	± 0.10	± 18	$1/8\lambda$	± 0.0005	± 0.05	-
L3	± 0.75	± 2.00	± 0.50	± 0.25	± 18	$1/8\lambda$	± 0.0005	± 0.05	-
L4	± 1.00	± 2.00	± 0.40	± 0.20	± 15	$1/8\lambda$	± 0.0005	± 0.05	-
L5	± 0.30	± 0.75	± 0.30	± 0.15	± 18	$1/8\lambda$	± 0.0005	± 0.03	-

Tolerance analysis

The above image quality, being obtained under the ideal optical system, might deteriorate due to material defects, fabrication errors, assembling and adjusting errors, mirror deformations caused by gravity and heat, and other factors in practical situation. During the optical design process, tolerance analysis is conducted to determine the detailed error limits on each optical element and system assembly. We use Monte Carlo analysis in Zemax Optic Studio to carry out tolerance analysis on the optical system at 0° zenith angle. In the analysis, Tolerance operands are defined in the tolerance data editor of Zemax Optic Studio. In each operand, initial tolerances are set according to practical experience from mechanical engineers, system engineers and vendors. The distance between the primary and secondary mirrors, and the distance between L5 and focal plane are set as compensators. Based on the initial tolerances, iterative optimization of the tolerances is carried out considering optical system performance (RMS spot radius is set as the performance criterion) and operational feasibility. Note that the value of tolerances would be adjusted during iteration according to the impacts of tolerances on the image quality. Table 4 shows the adjusted results of the assembly tolerance of the whole optical system. For the secondary mirror, position tolerance (DZ in Table 4), taking the primary mirror as a reference, is not more than ± 0.05 mm. The decenter tolerance in x and y direction (DX/DY in Table 4) should be both not more than ± 0.02 mm, while the tilt tolerance around x and y axis (TX/TY in Table 4) not more than ± 0.1 arcmin. The position tolerance of the lens L1 is not more than ± 0.50 mm, while the displacement and tilt errors are not more than ± 0.200 mm and ± 1.00 arcmin respectively. The position, decenter and tilt tolerances of other lenses are also listed in Table 4. The fabrication

tolerance of each optical element is displayed in Table 5, including the tolerances on surface curvature radius, thickness, surface decenter in x and y direction (DX/DY in Table 5), surface tilt around x and y axis (TX/TY in Table 5), surface accuracy, refraction index, abbe number and conic constant. It is worthy to mention that the tolerances having more impact on the image quality are given in the analysis and should be paid more attention to during manufacture and assembly, including the TX/TY tolerances of secondary mirror and lens L3, and the surface accuracy tolerance of the secondary mirror. After Monte Carlo analysis, the estimated RMS spot radius is 22.4 μm and is slightly worse than the maximum ideal RMS spot radius of 21.1 μm at 0° zenith angle. It indicates that the optical system still maintains acceptable image quality considering feasible material, fabrication, assembling, adjusting and other practical conditions.

Discussion

The optical design introduced in this work fully meets current requirements for MUST after considering the challenging manufacturing processes. Compared with other existing and future spectroscopic survey telescopes, MUST has the unique advantage of the critical performance of survey capability, which could be expressed in Eq. (5) [32].

$$\eta = A\Omega N f_{use} \theta^{-2} \tag{5}$$

where A represents the area of the primary mirror, Ω represents the area of the FOV, N represents the number of optical fibers in the focal plane, f_{use} represents the proportion of time used for the survey, and θ means the natural seeing at the telescope site. Note that the adopted equation is empirical and only provides a general and partial evaluation of a spectroscopic facility’s survey capability. It specifically focuses on the efficiency of a cosmological survey of large-scale structures. And a more accurate comparison of survey efficiencies depends on the exact scientific goals and many other factors, which is beyond the scope of this work. As shown in Table 6, MUST has a survey efficiency 19 times that of the DESI. It will become one of the largest and most advanced spectroscopic survey telescopes and make essential contributions to astrophysics and cosmology.

The Mirror Lab of the University of Arizona has cast the primary mirror, and the secondary mirror will be manufactured using a light-weighted design. As for the lenses of

Table 6 Survey performance of typical spectroscopic survey telescopes using the measure of Eq. (5) proposed by [32]

Telescope	Area of primary mirror (A/m ²)	Area of FOV (Ω/deg ²)	Number of optical fibers (N)	Proportion of time for survey (f_{use})	Seeing (θ/arcsec)	Index of survey capability (η/η _{DESI})
SDSS	4.91	7.1	1400	50%	1.40	0.044
4MOST ^a	13.20	4.0	2436	70%	0.80	0.497
DESI	12.57	7.5	5000	60%	1.00	1.000
MOONS ^a	52.81	0.14	1000	30%	0.80	0.012
Subaru	52.81	1.1	2400	25%	0.75	0.219
MUST	30.64	7.1	20000	70%	0.75	19.144

^a 4MOST 4-meter Multi-Object Spectroscopic, MOONS Multi-object Optical and Near-IR spectrograph

WFC, fused silica as the glass material is an easily available, uniform, and cost-effective choice that can ensure image quality and ease of manufacturing. The WFC has four aspherical surfaces with the maximum depth to remove less than 0.51 mm, comfortably within the manufacturer's capability. To our knowledge, lens L1, with a diameter of 1.8 m, is the largest corrector elements used in astronomy in the world. It will present additional challenges during the manufacturing and quality examination phases. According to the technical solutions currently discussed with the material provider, the lens blank of L1 can be contour ground from a single boule or reshaped from a smaller piece. The material provider, Corning, guarantees a refractive index inhomogeneity of 10 ppm, a birefringence of 2 nm/cm in the 1.8 m mirror blank. And Corning can achieve a Class 2 (0.50 mm maximum inclusion size) bubble/inclusion specification for this size mirror blank, even better than the standard Class 5 (1.27 mm maximum inclusion size). The refraction index is 1.45846 with a variation of ± 30 ppm and the abbe number is 67.82 with a possible variation of ± 0.01 . As for the secondary mirror, it is possible to add a central hole with a diameter of 120 mm to place a camera inside to monitor the end surfaces of the 20,000 optical fibers for high-precision positioning. However, other solutions for fiber view cameras exist, such as placing four cameras below the four wings of the spider around the secondary mirror. The final solution will be made based on a more careful evaluation.

To adjust the optical system with high precision, a set of wavefront sensors is designed to be installed on the focal plane. One wavefront sensor will be placed at the center of the focal plane, and six sensors will be put around the edge of the focal plane. They will jointly achieve full-aperture monitoring. During observation, this set of wavefront sensors will be used to track the aberration of the light in the optical system, and to correct the aberrations by adjusting the secondary mirror position and the forces applied to the primary mirror by the primary mirror support system.

The optical system model introduced here is based on the ideal situation. However, the actual image quality of the telescope can be affected by various factors, such as the defects in the manufactured lenses, the misalignment of the mirrors, the stress of the support system, gravity, dome seeing, and natural seeing. We will include these factors in our optical system models in future works. We will also update the model using new iteration criteria that can reflect these additional factors' influence on image quality. Based on this new model, we will implement a more feasible plan to adjust the design and improve the image quality. For example, once the impact of dome seeing can be reliably included in the model, we might be able to optimize the cooling and ventilation systems of the dome to improve the image quality further. Also, in our next work, the spatial temperature distribution and the thermal expansion coefficients of the support structure will be considered to build a more realistic model accounting for the thermal effect.

Conclusion

This paper presents the conceptual design of the optical system of the 6.5 m Multiplexed Survey Telescope (MUST) proposed by Tsinghua University. MUST will be constructed on the Saishiteng Mountain of Northwest China to carry out next-generation large-scale spectroscopic surveys. MUST adopts a compact R-C system

with a Cassegrain focus and a large WFC to facilitate the required high image quality and survey efficiency. Under the current design, the primary mirror is a 6.5 m honeycomb-shaped lightweight single mirror. The single mirror can improve image quality and reduce control complexity compared to a segmented mirror. The secondary mirror is a 2.45 m convex hyperboloid mirror. Combined with the concave hyperboloid primary mirror, they form the basic R–C optical system with a focal ratio of F/3.6 and a total focal length of 23323 mm. Along with the primary and secondary mirrors, a five-lens WFC design can improve image quality by compensating for atmospheric dispersion and wavefront aberration. After compensation, we achieved an excellent image quality with the EE80% diameter smaller than 0.6 arcsec for the entire 3° FOV and the whole 50° zenith angle range. After passing the primary mirror's 1.8 m diameter central hole, the targets' compensated light beam will be focused into high-quality image spots. They then enter the densely packed 20,000 optical fibers positioned at the focal plane, which are connected to the multi-object spectrographs. To our best knowledge, MUST will be one of the world's largest and most advanced spectroscopic survey telescopes. The lens L1 of its WFC, with a 1.8 m diameter, is almost certainly the largest transmissive corrector lens ever built. The breakthrough and innovation in the optical design will enable MUST to survey the northern sky 19 times more efficiently than the current world leader DESI survey. This design will help MUST become one of the world's largest and most advanced spectroscopic survey telescopes. It is reasonable to believe that MUST will advance our understanding of the universe significantly.

Abbreviations

FOV	Field of View
MUST	MULTIplexed Survey Telescope
DESI	Dark Energy Spectroscopic Instrument
SDSS	Sloan Digital Sky Survey
R–C	Ritchey-Chretien
EE80	80% Encircled Energy
MMT	Multiple Mirror Telescope
MSC	Metrology Camera System
PFS	Prime Focus Spectrograph
LAMOST	Large Sky Area Multi-Object Fiber Spectroscopic Telescope
WFC	Widefield Corrector
ADC	Atmospheric Dispersion Corrector
4MOST	4-m Multi-Object Spectroscopic
MOONS	Multi-object Optical and Near-IR Spectrograph

Acknowledgements

The authors sincerely thank the Richard F. Caris Mirror Lab, the University of Arizona, Corning Inc., Safran Reosc Inc., and Thales SESO S.A.S Inc. for their guidance and valuable insights during our iterative design discussion and process. We also sincerely thank Professor Xuefei Gong, Guoping Li, Xinnan Li and other experts from Nanjing Institute of Astronomical Optics & Technology, Chinese Academy of Sciences for their helpful discussion and important suggestions on the design and manufacture of the optical system, especially the multiple-element widefield corrector.

Authors' contributions

Y. Z.: Optical design, Simulation, Data analysis, Writing the original draft. H. J.: Optical design, Simulation, Data analysis. S. S.: Optical design, Simulation, Data analysis, Review. D. Y.: Design and Simulation of the Secondary mirror part. Z. C.: Introduction and Discussion, Data analysis, Review and Editing. Y. S.: Data analysis, Review and Editing. S. H.: Data analysis, Review and Editing. Y. Z.: Design and Simulation of the Primary mirror part. S. K.: Building the 3D model of the telescope. S. M.: Supervision the work, Review and Editing. L. H.: Data analysis, Review and Editing, Supervision of the work. The authors read and approved the final manuscript.

Funding

Supported by National key research and development program of China, Tsinghua University Initiative Scientific Research Program, Tsinghua University Education Foundation, Tsinghua-Jiangyin Innovation Special Fund (TJISF).

Availability of data and materials

The datasets used and analyzed during the current study are available from the corresponding author upon reasonable request.

Declarations**Ethics approval and consent to participate**

There is no ethics issue for this paper.

Consent for publication

All authors agreed to publish this paper.

Competing interests

The authors declare that they have no competing interests.

Received: 19 October 2022 Revised: 25 April 2023 Accepted: 4 May 2023

Published online: 19 May 2023

References

- Gilmozzi R, Jason S. The European extremely large telescope (E-ELT). *Messenger*. 2007;127(11):3.
- Tamai R, Cirusuolo M, González JC, Koehler B, Tuti M. The E-ELT program status. *Ground-based Airborne Telescopes VI* SPIE. 2016;9906:350–62.
- Cole G. Optical fabrication and metrology for the thirty meter telescope primary mirror segments. *Optical Fabrication and Testing*. 2017. <https://doi.org/10.1364/OFT.2017.OW1B.4>.
- Crampton D, Simard L. Instrument concepts and scientific opportunities for TMT. *Ground-based and Airborne Instrumentation for Astronomy*. SPIE. 2006. <https://doi.org/10.1117/12.669666>.
- Davila P, Wood HJ, Atcheson PD, Saunders R, Sullivan J, Vaughan AH, Saisse M. Telescope simulators for Hubble: an overview of optical designs. *Appl Opt*. 1993;32:1775–81.
- Leckrone DS. The Life and Times of the Hubble Space Telescope. *Frontiers in Optics*. 2008. <https://doi.org/10.1364/FIO.2008.STuA3>.
- Gunn JE, Siegmund WA, Mannery EJ, Owen RE, Hull CL, Leger RF, Carey LN, Knapp GR, York DG, Boroski WN, Kent SM, Lupton RH, Rockosi CM, Evans ML, Waddell P, Anderson JE, Annis J, Barentine JC, Bartoszek LM, Bastian S, Bracker SB, Brewington HJ, Briegel CI, Brinkmann J, Brown YJ, Carr MA, Czarapata PC, Drennan CC, Dombek T, Federwitz GR, Gillespie BA, Gonzales C, Hansen SU, Harvanek M, Hayes J, Jordan W, Kinney E, Klaene M, Kleinman SJ, Kron RG, Kresinski J, Lee G, Limmongkol S, Lindenmeyer CW, Long DC, Loomis CL, McGehee PM, Mantsch PM, Neilsen EH, Neswold RM, Newman PR, Nitta A, Peoples J, Pier JR, Prieto PS, Prosapio A, Rivetta C, Schneider DP, Snedden S, Wang S. The Sloan Digital Sky Survey. *Astron. J*. 2006; 131:2332–2359.
- Bundy K, Bershadly MA, Law DR, Yan R, Drory N, MacDonald N, Wake DA, Cherinka B, Sánchez-Gallego JR, Weijmans AM, Thomas D. Overview of the SDSS-IV MaNGA survey: mapping nearby galaxies at Apache Point observatory. *Astrophys. J*. 2014;798(7).
- Drory N, MacDonald N, Bershadly MA, Bundy K, Gunn J, Law DR, Smith M, Stoll R, Tremonti CA, Wake DA, Yan R, Weijmans AW, Byler N, Cherinka B, Cope F, Eigenbrot A, Harding P, Holder D, Huehnerhoff J, Jaehnig K, Jansen TC, Klaene M, Paat AM, Percival J, Sayres C. The MaNGA integral field unit fiber feed system for the Sloan 2.5 m telescope. *Astron. J*. 2015;149(77).
- Fabricant D, Fata RG, McLeod BA, Szentgyorgyi AH, Barberis J, Bergner HW, Brown WR, Caldwell N, Conroy MA, Eng R, Epps H, Furesz G, Gauron TM, Geary J, Goddard RE, Hartmann L, Hertz EN, Honsa M, Mueller M, Norton TJ, Ordway MP, Roll JB, Williams GG, Freedman-Woods DL, Zajac JM. The 6.5-m MMT's f/5 wide-field optics and instruments. *Ground-based Instrumentation for Astronomy*. SPIE. 2003; 5492:767–778.
- Williams GG. The MMT. Observatory: entering a new era of scientific discovery. *Ground-based Airborne Telescopes VII* SPIE. 2018;10700:907–15.
- Doel P, Sholl MJ, Liang M, Brooks D, Flaugher B, Gutierrez G, Kent S, Lampton M, Miller T, Sprayberry D. The DESI wide field corrector optics. *Ground-based and Airborne Instrumentation for Astronomy V*. SPIE. 2014; 9147:2124–2130.
- Jelinsky P, Wechsler R, Sharples R, Schubnell M, Rabinowitz D, Brooks D, Martini P, Besuner RW, Flaugher B, Levi ME, Rockosi C, Schlegel DJ, Sprayberry D, Bailey S, Doel P, Edelstein J, Honscheid K, Eisenstein D, Gutierrez G, Harris S, Poppett C, Silber JH, Joyce R, CardielSas L, Prada F, Kent S. Overview of the dark energy spectroscopic instrument. SPIE. 2018;10702:410–20.
- Tamura N, Takato N, Shimono A, Moritani Y, Yabe K, Ishizuka Y, Ueda A, Kamata Y, Aghazarian H, Arnouts S, Barban G, Barkhouser RH, Borges RC, Braun DF, Carr MA, Chabaud PY, Chang YC, Chen HY, Chiba M, Chou RCY, Chu YH, Cohen J, de Almeida RP, de Oliveira AC Sr, de Oliveira LS, de Oliveira LS, Dekany RG, Dohlen K, dos Santos JB, dos Santos LH, Ellis R, Fabricius M, Ferrand D, Ferreira D, Golebiowski M, Greene JE, Gunn JE Sr., Hammond R, Harding A, Hart M, Heckman TM, Hirata CJ, Ho P, Hope SC, Hovland L, Hsu SF, Hu YS, Huang PJ, Jaquet M, Jing Y, Karr J, Kimura M, King ME, Komatsu E, Le Brun V, Le Fèvre O, Le Fur A, Le Mignant D, Ling HH, Loomis CP, Lupton RH, Madec F, Mao P, Marrara LS, Mendes de Oliveira C, Minowa Y, Morantz C, Murayama H, Murray GJ, Ohyama Y, Orndorff J, Pascal S, Pereira JM, Reiley D, Reinecke M, Ritter A, Roberts M, Schwochert MA, Seiffert MD, Smees SA, Sodre L Jr, Spergel DN, Steinkraus AJ, Strauss MA, Surace C, Suto Y, Suzuki N, Swinbank J, Tait PJ, Takada M, Tamura T, Tanaka Y, Tresse L, Verducci O Jr, Vibert D, Vidal C, Wang SY, Wen CY, Yan CH, Yasuda N. Prime focus spectrograph (PFS) for the Subaru telescope: overview, recent progress, and future perspectives. SPIE. 2016;9908:456–472.

15. Tamura N, Takato N, Shimono A, Moritani Y, Yabe K, Ishizuka Y, Kamata Y, Ueda A, Aghazarian H, Arnouts S, Barkhouser RH, Balard P, Barette R, Belhadi M, Burnham JA, Caplar N, Carr MA, Chabaud PY, Chang YC, Chen HY, Chou CY, Chu YH, Cohen JG, de Almeida RP, de Oliveira AC, de Oliveira LS, Dekany RG, Dohlen K, dos Santos JB, dos Santos LH, Ellis RS, Fabricius M, Ferreira D, Furusawa H, Garcia-Carpio J, Golebiowski M, Gross J, Gunn JE, Hammond R, Harding A, Hart M, Heckman TM, Ho PTP, Hope SC, Hover DJ, Hsu SF, Hu YS, Huang PJ, Jamal S, Jaquet M, Jeschke E, Jing Y, Kado-Fong E, Karr JL, Kimura M, King ME, Koike M, Komatsu E, Le Brun V, Le Fèvre O, Le Fur A, Mignant DL, Ling HH, Loomis CP, Lupton RH, Madec F, Mao PH, Marchesini D, Marrara LS, Medvedev D, Mineo S, Minowa Y, Murayama H, Murray GJ, Ohyama Y, Onodera M, Orndorff J, Pascal S, Peebles J, Pernot G, Pourcelot R, Reiley DJ, Reinecke M, Roberts M, Rosa JA, Rousselle J, Schmitt A, Schwochert MA, Seiffert MD, Siddiqui H, Smees SA, Sodré Jr L, Steinkraus AJ, Strauss MA, Surace C, Tait PJ, Takada M, Tamura T, Tanaka M, Tanaka Y, Thakar AR, Jr OV, Vibert D, Wang SY, Wang Z, Wen CY, Werner S, Yamada Y, Yan CH, Yasuda N, Yoshida H, Yoshida M. Prime Focus Spectrograph (PFS) for the Subaru telescope: ongoing integration and future plans. *Ground-based and Airborne Instrumentation for Astronomy VII*. SPIE. 2018;10702:398–409.
16. Kaifu N. Subaru Telescope. *Advanced Technology Optical/IR Telescopes VI* SPIE. 1998;3352:14–22.
17. Cui XQ, Zhao YH, Chu YQ, Li GP, Li Q, Zhang LP, Su HJ, Yao ZQ, Wang YN, Xing XZ, Li XN, Zhu YT, Wang G, Gu BZ, Luo AL, Xu XQ, Zhang ZC, Liu GR, Zhang HT, Yang DH, Cao SY, Chen HY, Chen JJ, Chen KX, Chen Y, Chu JR, Feng L, Gong XF, Hou YH, Hu HZ, Hu NS, Hu ZW, Jia Lei1, Jiang FH, Jiang X, Jiang ZB, Jin G, Li AH, Li Y, Li YP, Liu GQ, Liu ZG, Lu WZ, Mao YD, Men L, Qi YJ, Qi ZX, Shi HM, Tang ZH, Tao QS, Wang DQ, Wang D, Wang GM, Wang H, Wang JN, Wang J, Wang JL, Wang JP, Wang L, Wang SQ, Wang Y, Wang YF, Xu LZ, Xu Y, Yang SH, Yu Y, Yuan H, Yuan XY, Zhai C, Zhang J, Zhang YX, Zhang Y, Zhao M, Zhou F, Zhou GH, Zhu J, Zou SC. The large sky area multi-object fiber spectroscopic telescope (LAMOST). *Res. Astron. Astrophys.* 2012;12(9):1197.
18. Zhao YH. Spectroscopic survey of LAMOS. *Ground-based and Airborne Telescopes V* SPIE. 2014;9145:439–44.
19. Cui XQ, Su DQ, Wang YN. Progress in the LAMOST optical system. *Optical Design, Materials, Fabrication, and Maintenance*. SPIE. 2000;4003:347–354.
20. Wang SG, Su DQ, Chu YQ, Cui XQ, Wang YN. Special configuration of a very large Schmidt telescope for extensive astronomical spectroscopic observation. *Appl Opt.* 1996;35:5155–61.
21. Bai ZR, Zhang HT, Yuan HL, Fan DW, He BL, Lei YJ, Dong YQ, Yu SC, Zhao YH, Zhang Y. The first data release of LAMOST low-resolution single-epoch spectra. *Res Astron Astrophys.* 2021;21(10):249.
22. Deng L, Yang F, Chen X, He F, Liu Q, Zhang B, Zhang CG, Wang K, Liu N, Ren AB, Luo ZQ, Yan ZZ, Tian JF, Pan J. Lenghu on the Tibetan Plateau as an astronomical observing site. *Nature.* 2021;596:353–6.
23. Eads R, Angel R. 6.5 m telescope for multi-object spectroscopy over a 3° field of view. *Appl. Opt.* 2020; 59:154–159.
24. Tan H, Ma D. Recommended optical system design for the SSST. *Appl Opt.* 2020;59(11):3508–17.
25. Bai H, Su DQ, Liang M, Shectman SA, Yuan XY, Cui XQ. Optical system research of multi-object fiber spectroscopic survey telescope. *Res Astron Astrophys.* 2021;21(6):132.
26. Wynne CG. Ritchey-Chretien telescopes and extended field systems. *ApJ.* 1968;152:675.
27. Dos Santos JB, de Oliveira AC, Gunn J, de Oliveira LS, de Arruda MV, Castilho B, Gneiding CD, Ribeiro FF, Murray G, Reiley DJ, Junior LS, de Oliveira CM. Studying focal ratio degradation of optical fibers for Subaru's prime focus spectrograph. *SPIE.* 2014;9151:1703–8.
28. Crause L, Bershady M, Buckley D. Investigation of focal ratio degradation in optical fibres for astronomical instrumentation. *SPIE.* 2008;7014:2194–204.
29. Ramsey LW. Focal ratio degradation in optical fibers of astronomical interest. *Fiber optics in astronomy*. 1988;3:26–39.
30. Smith WJ. *Modern optical engineering: the design of optical systems*. 4th ed. New York: McGraw-Hill; 2008.
31. Linyao Y, Qun W, Tianyi Z. Design of long focal infrared catadioptric optical system for multi-guided system. *CHIN OPT.* 2015;8(2):234–40.
32. Ellis RS, Bland-Hawthorn J, Bremer M, Brinchmann J, Guzzo L, Richard J, Rix HW, Tolstoy E, Watson D. The Future of Multi-Object Spectroscopy: a ESO Working Group Report. arXiv:1701.01976. <https://doi.org/10.48550/arXiv.1701.01976>.

Publisher's Note

Springer Nature remains neutral with regard to jurisdictional claims in published maps and institutional affiliations.

Submit your manuscript to a SpringerOpen® journal and benefit from:

- Convenient online submission
- Rigorous peer review
- Open access: articles freely available online
- High visibility within the field
- Retaining the copyright to your article

Submit your next manuscript at ► [springeropen.com](https://www.springeropen.com)